electronics

MDPI

Article

Large Signal Stability Analysis of Hybrid AC/DC Microgrids When a Single-Phase-to-Ground Fault Occurs

Xinbo Liu, Yake Zhang, Xiaotong Song and Yuntao Ju *

School of Electrical and Control Engineering, North China University of Technology, Beijing 100144, China; liuxinbo@ncut.edu.cn (X.L.); zhangyake2022@163.com (Y.Z.); songxt@ncut.edu.cn (X.S.)
* Correspondence: juyuntaomail@163.com

Abstract: Islanded hybrid AC/DC microgrids lack support for a large grid, and the negative incremental impedance of constant power loads (CPLs) aggravates the poor anti-disturbance capability of the system. When a single-phase ground fault (SPGF) occurs, the amount of fault impulse power that islanded AC/DC hybrid microgrids can stably withstand and when the protection equipment can work are both unknown. In this paper, the method of symmetrical components is utilized, and high-signal stability criteria for islanded hybrid AC/DC microgrids when a SPGF occurs are derived based on the mixed potential theory. The proposed criteria place quantitative constraints on the power of the PV unit, DC/AC converter current inner-loop proportional parameters, inductors, and inductor equivalent resistance, as well as energy storage unit power, CPL power, capacitors, DC bus voltage, line equivalent resistance, line equivalent inductance, equivalent inductance in the faulty branch, equivalent resistance in the faulty branch, positive-sequence equivalent impulse power of the SPGF, and zero-sequence equivalent impulse power. Furthermore, the maximum impulse power of a SPGF that islanded hybrid AC/DC microgrids could stably withstand is also presented, providing guidelines for protection equipment to decide when to work. In addition, the allowable maximum CPL power that islanded hybrid AC/DC microgrids could steadily support as a SPGF occurs is deduced, and the power is usually adopted to determine the states of an energy storage unit and load shedding in advance. Simulation and experimental validations prove the correctness of the derived high-signal stability criteria.

Keywords: islanded AC/DC hybrid microgrids; maximum impulse power of single-phase-to-ground fault (SPGF); constant power loads (CPLs); high-signal stability; mixed potential function

Citation: Liu, X.; Zhang, Y.; Song, X.; Ju, Y. Large Signal Stability Analysis of Hybrid AC/DC Microgrids When a Single-Phase-to-Ground Fault Occurs. *Electronics* **2024**, *13*, 1232. https://doi.org/10.3390/electronics13071232

Academic Editor: Ilan Aharon

Received: 6 February 2024
Revised: 19 March 2024
Accepted: 21 March 2024
Published: 26 March 2024

1. Introduction

Islanded AC/DC hybrid microgrids consist of various distributed generations (DGs), an AC bus, AC loads, a DC bus, DC loads, energy storage systems, and many interconnection converters, and they integrate both the advantages of AC microgrids and DC microgrids [1,2]. All tightly regulated converters and motors are regarded as constant power loads (CPLs), and the negative incremental impedance of CPLs might significantly increase disturbances and lead to instability [3–5]. The voltage and frequency of islanded AC/DC hybrid microgrids are usually supported by grid-forming converters replacing large grids. Furthermore, a large number of power electronic devices are utilized instead of traditional generators in microgrids, and small inertia and a poor anti-interference ability are both introduced [6,7]. Consequently, islanded AC/DC hybrid microgrids are extremely sensitive to disturbances. Actually, large severe disturbances are mostly caused by faults. Particularly, the single-phase ground fault (SPGF) accounts for the largest percentage of faults and is the most common [8–11]. However, when a SPGF occurs, the amount of fault impulse power that islanded AC/DC hybrid microgrids could stably withstand is unknown; when the protection equipment would work is not definite, and the amount of CPL power that islanded AC/DC hybrid microgrids could support is also not clear. To

avoid a blackout, it is very important to determine how to guarantee the stable operation of islanded AC/DC hybrid microgrids when an SPGF occurs [12,13].

In fact, the transient stability analysis of power systems under fault conditions is widely performed [14–16]. References [14,15] studied the transient stability of permanent magnet synchronous generators and doubly fed wind turbines when severe grid faults appeared. Reference [16] considered the transient stability of voltage source converters with adaptive phase-locked loops under grid fault and fault recovery conditions. Based on the data distribution of transient zero-sequence currents, reference [17] detected a SPGF under three-phase voltage imbalance conditions in neutral inefficiently grounded distribution systems. Reference [18] proposes a novel SPGF detection method according to single-phase instantaneous reactive power theory and instantaneous active power theory to discriminate the line state. Reference [19] analyzed the SPGF characteristics in modular multilevel converter-based high-voltage direct-current (MMC-HVDC) converter stations and proposed an overvoltage suppression stabilization control strategy based on zero-sequence voltage modulation. These studies propose many mature methods to increase the stability for large power systems under various fault conditions, especially SPGF. Unfortunately, due to the small inertia and poor anti-interference ability of microgrids, these mature methods are not applicable to analyzing microgrids' stability under fault conditions.

Investigating the stability of microgrids while considering fault influences is particularly important. When severe three-phase symmetrical faults appear, the synchronization stability of grid-connected converters under weak grid conditions has been described [20]. Reference [21] proposes the fault ride-through (FRT) control for voltage-controlled inverters in distributed generation units. Obviously, faults significantly affect the stability of islanded microgrids without the support of large grids. Reference [22] studied the stability of islanded microgrids with shunt synchronous generators and virtual synchronous generators (SG-VSGs) when three-phase short-circuit faults occur. Reference [23] presents current- and voltage-limiting strategies to enhance the fault ride-through (FRT) capability of islanded microgrids under symmetrical and asymmetrical fault conditions. Reference [24] explores the fundamental issues of converter control for islanded microgrids under faulty conditions. In [25], a superimposed phase current scheme with voltage constraint elements is proposed for identifying faults in islanded microgrids. In [26], a self-propelled artillery fault line identification method based on the construction of high-frequency zero-sequence voltage and zero-sequence current is proposed for islanded microgrids. The mentioned studies are all focused on fault identification and converter control, and the typical characteristics of CPLs are not taken into account. Furthermore, it is extremely necessary to consider the fault influences, the micro source features, the CPLs, and the energy storage during microgrid stability analysis procedures.

On the other side, a high-signal stability analysis is the most typical stability method for microgrids. Based on the Lyapunov function, a high-signal stability criterion of DC microgrids is derived in [27]. Reference [28] also utilized the Lyapunov function to construct a high-signal model of microgrids and obtained an asymptotic stability domain to illustrate parameter stability influences. Reference [29] constructed the neural Lyapunov function of microgrids and obtained the stability region. Reference [30] optimized the polynomial droop controller and estimated the operation region for DC microgrids. Reference [31] approximated the nonlinear model of microgrids with a TS fuzzy model and obtained the stability domain using an LMI tool. Particularly, the Brayton–Moser mixed potential function method is generally adopted to analyze the high-signal stability of microgrids. For AC/DC hybrid microgrids, reference [32] derived and optimized a unified stability criterion while considering the battery operation mode and the converter output current limitation based on the mixed potential function. References [33,34] present an absolute stability condition and a region of asymptotic stability of DC microgrids using the mixed potential function. As mentioned, the characteristics of CPLs, energy storage units, and

converter parameters are all considered in the high-signal stability of microgrids; however, the fault influences are not taken into account.

When a SPGF occurs, asymmetrical effects are introduced to the microgrids; consequently, the modeling of the islanded AC/DC hybrid microgrids becomes quite difficult. In this paper, to guarantee the stability operation of islanded AC/DC hybrid microgrids when a SPGF occurs, the method of symmetrical components is used, and large-signal stability criteria are derived based on mixed potential theory. The positive-sequence power of the PV unit, DC/AC converter current inner-loop proportional parameters, inductors, and inductor equivalent resistance, as well as energy storage unit power, CPL power, capacitors, DC bus voltage, the line equivalent resistance, line equivalent inductance, the equivalent inductance in the faulty branch, the equivalent resistance in the faulty branch, the positive-sequence equivalent impulse power of the SPGF, and zero-sequence equivalent impulse power are all considered. The contributions of this paper are summarized as follows:

(1) Based on the structure and control strategies, the method of symmetrical components is utilized, and the positive-sequence equivalent model and zero-sequence equivalent model of islanded AC/DC hybrid microgrids when a SPGF occurs are derived in the dq rotating frame separately.
(2) Large signal stability criteria of islanded hybrid AC/DC microgrids when a SPGF occurs are obtained using mixed potential theory.
(3) The maximum impulse power of a SPGF that islanded hybrid AC/DC microgrids could stably suffer is derived and provides quantitative guidelines for protection equipment to decide when to work.
(4) The allowable maximum CPL power that islanded hybrid AC/DC microgrids could stably support as a SPGF occurs is deduced, and the power is usually adopted to determine the power of the energy storage unit and load shedding in advance.

2. Equivalent Modeling of Islanded AC/DC Hybrid Microgrids

2.1. Structure and Control Strategies of Islanded AC/DC Hybrid Microgrids

A representative islanded AC/DC hybrid microgrid is shown in Figure 1. The PV generation unit, the energy storage unit, a bidirectional DC/AC converter, CPLs, and resistive loads are all included. The energy storage unit is composed of a buck–boost converter and batteries and is connected to the AC bus through the cascaded bidirectional DC/AC converter. The CPLs are represented by a closed loop-controlled buck converter and a resistor, and the power consumption of the CPLs is constant.

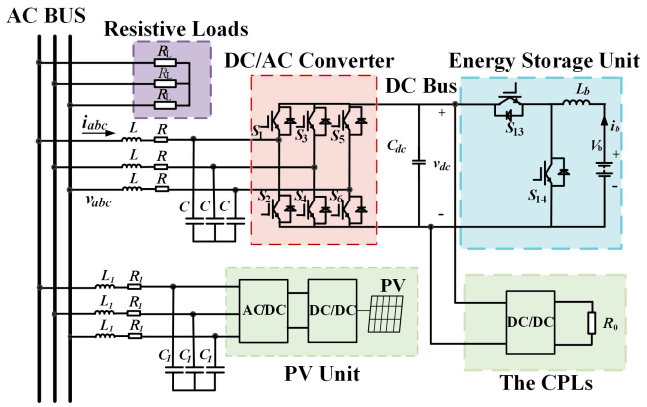

Figure 1. The structure of islanded AC/DC hybrid microgrids.

DC/DC converters cascaded with AC/DC converters are utilized in PV units. The DC/DC converter boosts the DC voltage, and the AC/DC converter achieves the power output.

The control flow of the bidirectional buck–boost converter in the energy storage unit is shown in Figure 2. The PI control strategies are utilized in both the outer voltage controllers

and inner current controllers. When i_b is positive, the battery is working in a discharging state, and when i_b is negative, the battery is working in a charging state. Firstly, the reference voltage v_{dcref} and the actual voltage v_{dc} are compared. If the battery is in a discharging state, and the calculated reference current i_{bref} of the battery is positive, and when $v_{dcref} > v_{dc}$ occurs, i_{bref} is increased to maintain v_{dc} equal to v_{dcref}. On the contrary, if the battery is in a charging state, and the calculated reference current i_{bref} of the battery is negative, and when $v_{dcref} > v_{dc}$, i_{bref} is also increased, the absolute value of the charging current i_{bref} is decreased to increase the DC bus. Furthermore, when $v_{dcref} < v_{dc}$, similar regulation procedures are also performed.

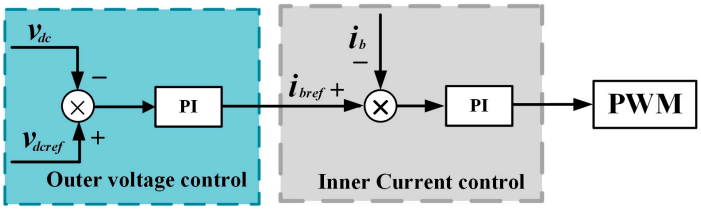

Figure 2. The control flow of the bidirectional buck–boost converter in the energy storage unit.

The control flow of the bidirectional DC/AC converter is shown in Figure 3. Q/V and P/f droop controls are used to obtain the reference voltages v_{dref} and v_{qref} at the d-axis and q-axis, respectively. The abc-dq and dq-abc coordinate transformations are both adopted. Actual AC voltage v_{abc} and current i_{abc} are used to obtain active power p and reactive power q. Outputs of the low-pass filter are $\overline{p}$ and $\overline{q}$, respectively, and m and n are the droop coefficients. P_n, Q_n, f_n, and V_n are the reference active power, reference reactive power, reference frequency, and reference voltage, respectively. The v_d and v_q are actual voltages at the d-axis and q-axis, respectively. The i_{dref} and i_{qref} are the reference currents at the d-axis and q-axis, respectively. The i_d and i_q are actual currents at the d-axis and q-axis, respectively. The k_{ip} and k_{ii} are proportionality and integration coefficients of the inner current loop. The relationship of the inner current loop is shown as (1).

$$\begin{cases} v_d = -\left\{k_{ip}\left(i_{dref} - i_d\right) + k_{ii}\int\left(i_{dref} - i_d\right)dt\right\} + \omega L i_q \\ v_q = -\left\{k_{ip}\left(i_{qref} - i_q\right) + k_{ii}\int\left(i_{qref} - i_q\right)dt\right\} - \omega L i_d \end{cases} \quad (1)$$

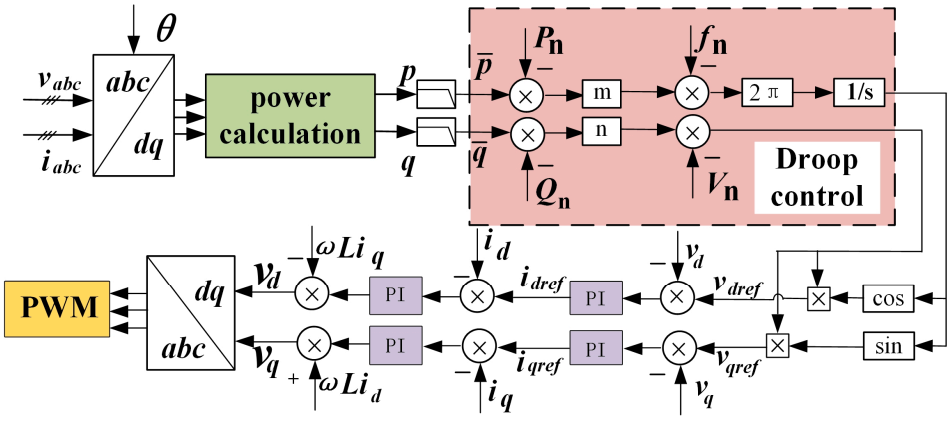

Figure 3. The control flow of the bidirectional DC/AC converter.

2.2. The Model of CPLs, PV Units, and Energy Storage Units

The current and voltage of CPLs are i and v, respectively. The power consumption of CPLs is P_0, and the model of the CPLs is shown in Figure 4.

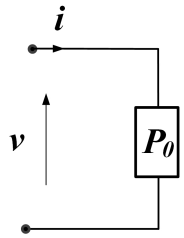

Figure 4. The model of CPLs.

The PV unit is modeled as a power source, and the power is PG, shown in Figure 5. The control strategy of the two photovoltaic power generation units on the AC side is the same. The output power of P_G is always positive, and is not negative.

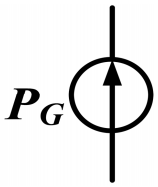

Figure 5. The equivalent model of PV unit.

The batteries and cascaded buck–boost converter are modeled as a power source, and the power is P_b, shown in Figure 6. If P_b is positive, the batteries are discharging. On the contrary, if P_b is negative, the batteries are charging.

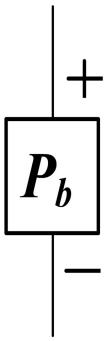

Figure 6. The equivalent model of batteries and cascaded buck–boost converter.

2.3. The Equivalent Model of Bidirectional DC/AC Converter in dq Rotating Frame

The traditional topology of a bidirectional DC/AC converter is shown in Figure 7. $e_{k(t)}$ ($k = a, b, c$) are the voltages of the three-phase AC source, L denotes the equivalent inductance of the line, R denotes the equivalent resistance of the line, C_{dc} is the DC capacitor, R_{L} is the resistive load, and v_{dc} denotes the DC bus voltage.

The switching function s_k is introduced and is defined as:

$$s_k = \begin{cases} 1 \text{ the upper device} \\ 0 \text{ the lower device} \end{cases} \tag{2}$$

The bidirectional DC/AC converter is expressed as:

$$\begin{cases} L\frac{di_a}{dt} + Ri_a = e_a - (v_{dc}s_a + v_{NO}) \\ L\frac{di_b}{dt} + Ri_b = e_b - (v_{dc}s_b + v_{NO}) \\ L\frac{di_c}{dt} + Ri_c = e_c - (v_{dc}s_c + v_{NO}) \end{cases} \tag{3}$$

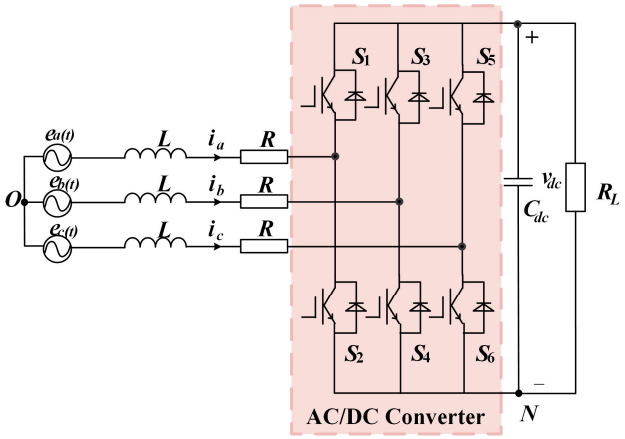

Figure 7. Traditional topology of the bidirectional DC/AC converter.

The abc-dq coordinate transformation is utilized, and the transformation matrix is shown as follows:

$$C_{3s2r} = \frac{2}{3}\begin{bmatrix} \sin\omega t & \sin\left(\omega t - \frac{2\pi}{3}\right) & \sin\left(\omega t + \frac{2\pi}{3}\right) \\ \cos\omega t & \cos\left(\omega t - \frac{2\pi}{3}\right) & \cos\left(\omega t + \frac{2\pi}{3}\right) \end{bmatrix} \tag{4}$$

The mathematical model of the DC/AC converter is as follows:

$$\begin{cases} C\frac{dv_{dc}}{dt} = \frac{3}{2}\left(i_q s_q + i_d s_d\right) - i_L \\ L\frac{di_d}{dt} - \omega L i_q + R i_d = e_d - v_{dc} s_d \\ L\frac{di_q}{dt} + \omega L i_d + R i_q = e_d - v_{dc} s_q \end{cases} \tag{5}$$

This paper considers the condition that the power factor is 1. Let $v_d = s_d v_{dc}$ and $v_q = s_q v_{dc}$, according to the principle of power conservation, and $i_q = 0$; then, the DC current i_0 is obtained from (5) and is expressed as follows:

$$i_0 = \frac{v_d i_d}{v_{dc}} \tag{6}$$

Based on (6) and Figure 7, the equivalent model of a bidirectional DC/AC converter in a dq rotating frame on the condition that the power factor is 1 is obtained and shown in Figure 8.

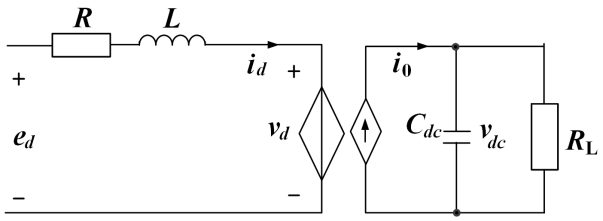

Figure 8. The equivalent model of a bidirectional DC/AC converter in a dq rotating frame on the condition that the power factor is 1.

2.4. The Equivalent Model of Islanded AC/DC Hybrid Microgrids in DQ Rotating Frame

Based on the equivalent models of Figures 4–6 and 8, the equivalent model of the islanded AC/DC microgrids in Figure 1 is obtained and shown in Figure 9. The PV unit is modeled as a power source, P_{G1} or P_{G2}. L_1 denotes the line equivalent inductance, and R_1 is the parasitic resistance of the line. R_L is the AC resistive load. L_s and C_s are the AC filter parameters of the bidirectional DC/AC converter, and R_s is the parasitic resistance of the

inductor. C_{dc} is the DC capacitor. The power consumption of the CPLs is P_0. The power of the energy storage unit is P_b. The positive or negative values of P_b indicate the discharging or charging states of batteries.

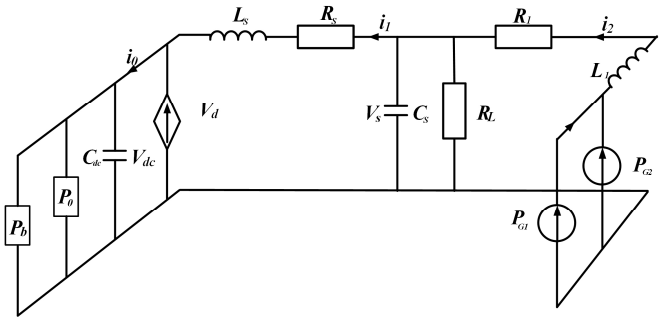

Figure 9. The equivalent model of islanded AC/DC hybrid microgrids.

The equivalent model of the islanded AC/DC hybrid microgrids in Figure 9 is only applicable to symmetrical systems. Unfortunately, when a SPGF occurs, islanded AC/DC hybrid microgrids are unsymmetrical. How to derive the equivalent model of islanded AC/DC hybrid microgrids when SPGF occurs becomes a big issue.

2.5. The Equivalent Model of Islanded Hybrid AC/DC Microgrids When SPGF Occurs

The method of symmetrical components describes unsymmetrical three-phase vectors that could be decomposed into three symmetrical vectors, and these symmetrical vectors are unique. Consequently, the method of symmetrical components is usually used for unsymmetrical systems to obtain symmetric components in positive-sequence, negative-sequence, and zero-sequence separately [35].

When a SPGF occurs, based on the method of symmetrical components, positive-sequence components, zero-sequence components, and negative-sequence components of hybrid AC/DC microgrids are all derived, respectively.

As shown in Figure 9, when a SPGF occurs in phase A of P_{G1}, the power injecting the ground fault point is S_p and is shown as follows:

$$S_p = P_A + P_B + P_C = \mathrm{Re}\left(\begin{bmatrix} V_A & V_B & V_C \end{bmatrix} \begin{bmatrix} I_A \\ I_B \\ I_C \end{bmatrix}^* \right) = {V_P}^{\mathrm{T}} {I_P}^* \tag{7}$$

In (7), V_A, V_B, and V_C are three-phase fault voltages, $V_P^{\mathrm{T}} = \begin{bmatrix} V_A & V_B & V_C \end{bmatrix}$, I_A, I_B, and I_C are three-phase fault injection currents, $I_P^{\mathrm{T}} = \begin{bmatrix} I_A & I_B & I_C \end{bmatrix}$, $S_p = \mathrm{Re}[V_A {I_A}^* + V_B {I_B}^* + V_C {I_C}^*]$, T represents the matrix transpose, * represents the phase conjugate, and Re denotes the real part of S.

The conversion matrix from voltages to sequential components is shown as follows:

$$\begin{bmatrix} V^P \\ V^N \\ V^0 \end{bmatrix} = \frac{1}{3} \begin{bmatrix} 1 & a & a^2 \\ 1 & a^2 & a \\ 1 & 1 & 1 \end{bmatrix} \begin{bmatrix} V_a \\ V_b \\ V_a \end{bmatrix} \tag{8}$$

The superscripts P, N, and 0 indicate positive-sequence, negative-sequence, and zero-sequence, respectively; $a = \mathrm{e}^{\mathrm{j}120^\circ}$.

Based on (7), the relationships are obtained as follows:

$$\begin{aligned} S_P &= \mathrm{Re}\left(V_A I_A^* + V_B I_B^* + V_C I_C^*\right) = \mathrm{Re}\left[3V^P \left(I^P\right)^* + 3V^N \left(I^N\right)^* + 3V^0 \left(I^0\right)^*\right] \\ &= P^P + P^N + P^0 \end{aligned} \tag{9}$$

Islanded hybrid AC/DC microgrids are often three-phase, three-wire systems; when a SPGF occurs in phase A of the PV unit, the voltage and current vectors of the grounding point are shown in Figure 10.

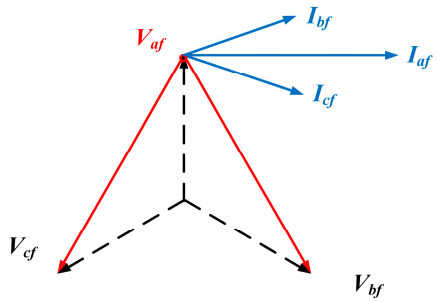

Figure 10. The voltage and current vectors of the grounding point when phase A is grounded.

The voltages and currents of the SPGF point are as follows:

$$\begin{bmatrix} V_{af} \\ V_{bf} \\ V_{cf} \end{bmatrix} = \begin{bmatrix} 0 \\ \sqrt{3}V_a e^{j-\frac{5}{6}\pi} \\ \sqrt{3}V_a e^{j\frac{5}{6}\pi} \end{bmatrix}, \begin{bmatrix} I_{af} \\ I_{bf} \\ I_{cf} \end{bmatrix} = \begin{bmatrix} 3I_a e^{j-\frac{1}{2}\pi} \\ \sqrt{3}I_a e^{j-\frac{1}{3}\pi} \\ \sqrt{3}I_a e^{j-\frac{2}{3}\pi} \end{bmatrix} \tag{10}$$

Based on (8)–(10), the following are derived:

$$\begin{bmatrix} V^P \\ V^N \\ V^0 \end{bmatrix} = \frac{1}{3}\begin{bmatrix} 1 & 1 & 1 \\ a^2 & a & 1 \\ a & a^2 & 1 \end{bmatrix}\begin{bmatrix} 0 \\ \sqrt{3}V_A e^{j-\frac{5}{6}\pi} \\ \sqrt{3}V_A e^{j\frac{5}{6}\pi} \end{bmatrix} = \begin{bmatrix} V_A e^{j0} \\ 0 \\ V_A e^{j\pi} \end{bmatrix} \tag{11}$$

$$\begin{bmatrix} I^P \\ I^N \\ I^0 \end{bmatrix} = \frac{1}{3}\begin{bmatrix} 1 & 1 & 1 \\ a^2 & a & 1 \\ a & a^2 & 1 \end{bmatrix}\begin{bmatrix} 3I_A e^{j-\frac{1}{2}\pi} \\ \sqrt{3}I_A e^{j-\frac{1}{3}\pi} \\ \sqrt{3}I_A e^{j-\frac{2}{3}\pi} \end{bmatrix} = \begin{bmatrix} \sqrt{2}I_A e^{j-\frac{3}{4}\pi} \\ I_A e^{j-\frac{1}{2}\pi} \\ 2I_A e^{j-\frac{1}{2}\pi} \end{bmatrix} \tag{12}$$

The negative-sequence voltage of the SPGF point is zero, and consequently, the fault impulse power of the fault point is only related to the positive-sequence power P^P and zero-sequence power P^0, and it is shown as follows:

$$S_p = 3\begin{bmatrix} V^P & V^N & V^0 \end{bmatrix}\begin{bmatrix} I^P \\ I^N \\ I^0 \end{bmatrix}^* = P^P + P^0 \tag{13}$$

Based on (13) and the equivalent model in Figure 9, the positive-sequence equivalent model of the islanded AC/DC hybrid microgrids when a SPGF occurs is derived and shown in Figure 11. L_f is the equivalent inductance of the faulty branch, and C_f is the equivalent capacitance of the faulty branch.

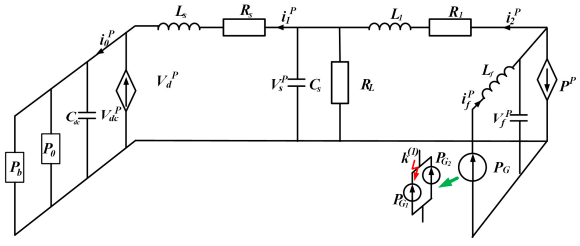

Figure 11. The positive-sequence equivalent model of islanded AC/DC hybrid microgrids when SPGF occurs. The red arrows in the figure indicate where SPGF occurs, and the green arrows indicate that P_{G1} and P_{G2} on the right are obtained from P_G equivalent.

Similarly, the zero-sequence equivalent model of the islanded AC/DC hybrid microgrid when a SPGF occurs is derived. The equivalent resistance in the faulty branch is R_g, the equivalent inductance in the faulty branch is L_g, the capacitance in the faulty branch is C_g, and the voltage is ${V_g}^0$. Based on (13) and the equivalent model in Figure 9, the zero-sequence equivalent model of the islanded hybrid AC/DC microgrids is shown in Figure 12.

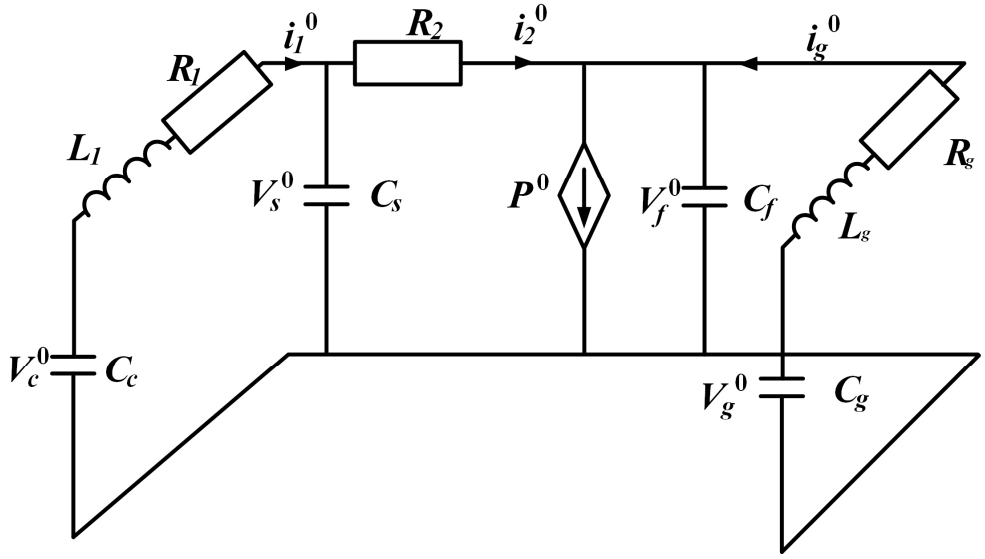

Figure 12. The zero-sequence equivalent model of islanded AC/DC hybrid microgrid when SPGF occurs.

3. Large-Signal Stability Analysis of an Islanded AC/DC Hybrid Microgrid When SPGF Occurs

The mixed potential theory is utilized to analyze the stability of islanded hybrid AC/DC microgrids when a SPGF occurs. Firstly, this theory is simply demonstrated. Then, the large-signal model and stability criterion for the positive-sequence equivalent model in Figure 11 are derived. Next, a large-signal model and stability criterion for the zero-sequence equivalent model in Figure 12 are proposed. Finally, the combined stability criteria for the islanded hybrid AC/DC microgrids when a SPGF occurs are obtained.

3.1. The Mixed Potential Function Theory

The mixed potential theory was proposed by R.K. Rayton and J.K. Mercer in 1964 and is widely used to analyze large-signal stability of nonlinear systems [36]. The mixed potential function is a special form of Lyapunov functions [37–39]. For nonlinear circuits with different structures, the unified form of mixed potential function is as follows:

$$P(i, v) = -A(i) + B(v) + (i, \gamma v - \alpha) \tag{14}$$

In (14), $A(i)$ is the current potential function, $B(v)$ is the voltage potential function, and $(i, \gamma v - \alpha)$ depends on the system topology.

Verify the correctness of (14) by (15).

$$\begin{cases} L\frac{\mathrm{d}i_\rho}{\mathrm{d}t} = \frac{\partial P(i,v)}{\partial i_\rho} \\ C\frac{\mathrm{d}v_\sigma}{\mathrm{d}t} = -\frac{\partial P(i,v)}{\partial v_\sigma} \end{cases} \tag{15}$$

In (15), P is the mixed potential function, and L is the inductances in the circuit. C are the capacitances in the circuit, v_σ are the capacitance voltages, and i_σ are the inductance currents.

The third stability theorem of mixed potential theory is often utilized to derive large-signal criteria. Further, μ_1 is the minimum eigenvalue of $L^{-1/2}A_{ii}(i)\,L^{-1/2}$, and μ_2 is the

minimum eigenvalue of $C^{-1/2}B_{uu}(u)\ C^{-1/2}$, $A_{ii}(i) = \partial^2 A(i)/\partial i^2$, $B_{vv}(v) = \partial^2 B(v)/\partial v^2$, $P_i = \partial P(i,v)/\partial i$, and $P_v = \partial P(i,v)/\partial v$.

If (16) is satisfied, then there exists a convergence region where the system trajectory converges to the steady-state equilibrium operating point.

$$\mu_1 + \mu_2 \geq \delta, \delta > 0 \tag{16}$$

3.2. Large Signal Model and Stability Criterion for Positive-Sequence Equivalent Model of Islanded Hybrid AC/DC Microgrids

Define currents and voltage variables according to the positive-sequence equivalent model in Figure 11.

$$i = \begin{bmatrix} i_1^P & i_2^P & i_f^P \end{bmatrix}, v = \begin{bmatrix} v_s^P & v_{dc}^P & v_f^P \end{bmatrix} \tag{17}$$

The current function ${P_i}^P$ associated with the current variables is as follows:

$$P_i^P = -\frac{1}{2}\left(i_2^P\right)^2 R_1 - \frac{1}{2}\left(i_1^P\right)^2 R_s - v_d^P i_1^P + \int_0^{i_f^P} \frac{P_G}{i} di \tag{18}$$

The voltage function ${P_v}^P$ associated with the voltage variables is as follows:

$$\begin{array}{l} P_v^P = i_0^P v_{dc}^P - \int_0^{v_{dc}^P} i_0^P dv + P_b - \int_0^{v_{dc}^P} \frac{P_b}{v} dv - P_0 + \\ \int_0^{v_{dc}^P} \frac{P_0}{v} dv - \frac{1}{2}\frac{\left(v_s^P\right)^2}{R_L} - P^P + \int_0^{v_f^P} \frac{P^P}{v} dv \end{array} \tag{19}$$

The powers of capacitors C_s, C_{dc}, and C_f are denoted as P_{Cs}, P_{Cdc}, and P_{Cf}, respectively, and shown as follows:

$$\begin{cases} P_{C_s}^P = i_2^P v_s^P - \left(v_s^P\right)^2 / R_L - i_1^P v_s^P \\ P_{C_{dc}}^P = i_0^P v_{dc}^p - P_0 + P_b \\ P_{C_f}^P = i_f^P v_f^P - P^P - i_2^P v_f^P \end{cases} \tag{20}$$

Combining (18)–(20), the mixed potential function $P(i^P,v^P)$ based on the positive-sequence equivalent model in Figure 11 is achieved and shown as follows:

$$\begin{array}{l} P(i^P, v^P) = -\frac{1}{2}\left(i_2^P\right)^2 R_1 - \frac{1}{2}\left(i_1^P\right)^2 R_s - v_d^P i_1^P - \int_0^{v_{dc}^P} \frac{P_b}{v} dv + \int_0^{v_{dc}^P} \frac{P_0}{v} dv + \\ \int_0^{i_f^P} \frac{P_G}{i} di + \frac{1}{2}\frac{\left(v_s^P\right)^2}{R_L} + \int_0^{v_f^P} \frac{P^P}{v} dv - \int_0^{v_{dc}^P} i_0^P dv - i_2^P v_s^P + i_1^P v_s^P - i_f^P v_f^P + i_2^P v_f^P \end{array} \tag{21}$$

The current potential function $A(i^P)$ is as follows:

$$A\left(i^P\right) = \begin{bmatrix} \frac{1}{2}\left(i_1^P\right)^2 R_s + v_d^P i_1^P & 0 & 0 \\ 0 & \frac{1}{2}\left(i_2^P\right)^2 R_1 & 0 \\ 0 & 0 & -\int_0^{i_f^P} \frac{P_G}{i} di \end{bmatrix} \tag{22}$$

The voltage potential function $B(v^P)$ is as follows:

$$B\left(v^P\right) = \begin{bmatrix} \frac{1}{2}\frac{\left(v_s^P\right)^2}{R_L} & 0 & 0 \\ 0 & -\int_0^{v_{dc}^P} \frac{P_b}{v} dv + \int_0^{v_{dc}^P} \frac{P_0}{v} dv - \int_0^{v_{dc}^P} i_0^P dv & 0 \\ 0 & 0 & \int_0^{v_f^P} \frac{P^P}{v} dv \end{bmatrix} \tag{23}$$

In order to verify the correctness of (21), a derivation based on Figure 11 and Equation (15) is carried out as follows.

$$\begin{cases} \frac{dP(i,v)}{di_1^P} = -i_1^P R_s - v_d^P + v_s^P = L_s \frac{di_1^P}{dt} \\ \frac{dP(i,v)}{di_2^P} = -i_2^P R_1 - v_s^P + v_f^P = L_1 \frac{di_2^P}{dt} \\ \frac{dP(i,v)}{di_f^P} = \frac{P_G}{i_f^P} - v_f^P = L_f \frac{di_f^P}{dt} \\ \frac{dP(i,v)}{dv_s^P} = \frac{v_s^P}{R_L} - i_2^P + i_1^P = -C_s \frac{dv_s^P}{dt} \\ \frac{dP(i,v)}{dv_f^P} = \frac{P^P}{v_f^P} - i_f^P + i_2^P = -C_f \frac{dv_f^P}{dt} \\ \frac{dP(i,v)}{dv_{dc}^P} = -i_0^P - \frac{P_b}{v_{dc}^P} + \frac{P_0}{v_{dc}^P} = -C_{dc} \frac{dv_{dc}^P}{dt} \end{cases} \tag{24}$$

Formula (24) satisfies (15), and the mixed potential function in (21) is correct.

According to (22) and (23), $A_{ii}(i^P)$ and $B_{vv}(v^P)$ are obtained, respectively, and are shown as follows:

$$A_{ii}\left(i^P\right) = \begin{bmatrix} R_s + \frac{\partial v_d}{\partial i_1} & 0 & 0 \\ 0 & R_1 & 0 \\ 0 & 0 & P_G / \left(i_f^P\right)^2 \end{bmatrix} \tag{25}$$

$$B_{vv}(v^P) = \begin{bmatrix} \frac{1}{R_L} & 0 & 0 \\ 0 & \frac{P_b - P_0}{\left(v_{dc}^P\right)^2} & 0 \\ 0 & 0 & -\frac{P^P}{\left(v_f^P\right)^2} \end{bmatrix} \tag{26}$$

According to the closed-loop control strategy in (1), the partial derivative of v_d with respect to i_d is calculated and is as follows:

$$\frac{\partial v_d}{\partial i_1} = \frac{\partial v_d}{\partial i_d} = k_{ip} + k_{ii} t \tag{27}$$

In (27), k_{ip} and k_{ii} are proportional and integral parameters of the current inner loop for a bidirectional DC/AC converter. Furthermore, k_{ii} has unpredictable dynamic characteristics during dynamic procedures due to its own delay characteristics, and for simplification, (27) is transformed as follows:

$$\frac{\partial v_d}{\partial i_1} = \frac{\partial v_d}{\partial i_d} = k_{ip} \tag{28}$$

Actually, i_d in Figure 3 and i_1 in Figure 11 are the same. Based on (28), (25) is transformed into

$$A_{ii}\left(i^P\right) = \begin{bmatrix} R_s + k_{ip} & 0 & 0 \\ 0 & R_1 & 0 \\ 0 & 0 & P_G / \left(i_f^P\right)^2 \end{bmatrix} \tag{29}$$

According to Figure 11, (26) and (29), the following are obtained and shown as follows:

$$L^{-1/2} A(ii) L^{-1/2} = \begin{bmatrix} \frac{R_s + k_{ip}}{L_s} & 0 & 0 \\ 0 & \frac{R_1}{L_1} & 0 \\ 0 & 0 & \frac{P_G}{\left(i_f^P\right)^2 L_f} \end{bmatrix} \tag{30}$$

$$C^{-1/2}B(vv)C^{-1/2} = \begin{bmatrix} \frac{1}{R_L C_s} & 0 & 0 \\ 0 & \frac{P_b - P_0}{\left(v_{dc}^P\right)^2 C_{dc}} & 0 \\ 0 & 0 & -\frac{P^P}{\left(v_f^P\right)^2 C_f} \end{bmatrix} \tag{31}$$

Based on mixed potential theory, μ_1 is the smallest eigenvalue of $L^{-1/2}A(ii)\,L^{-1/2}$, and μ_2 is the smallest eigenvalue of $C^{-1/2}B\,(vv)\,C^{-1/2}$. μ_1 and μ_2 are as follows:

$$\begin{cases} \mu_1 = \min\left[\frac{R_s + k_{ip}}{L_s} \quad \frac{R_1}{L_1} \quad \frac{P_G}{\left(i_f^P\right)^2 L_f} \right] \\ \mu_2 = \min\left[\frac{1}{R_L C_s} \quad \frac{P_b - P_0}{\left(v_{dc}^P\right)^2 C_{dc}} \quad -\frac{P^P}{\left(v_f^P\right)^2 C_f} \right] \end{cases} \tag{32}$$

According to (16), the large-signal stability criterion for a positive-sequence equivalent model of the islanded hybrid AC/DC microgrids is as follows:

$$\min\left\{ \frac{R_s + k_{ip}}{L_s}, \frac{R_1}{L_1}, \frac{P_G}{\left(i_f^P\right)^2 L_f} \right\} + \min\left\{ \frac{1}{R_L C_s}, \frac{P_b - P_0}{\left(v_{dc}^P\right)^2 C_{dc}}, -\frac{P^P}{\left(v_f^P\right)^2 C_f} \right\} > 0 \tag{33}$$

Based on (33), the simplified stability criterion is shown as follows:

$$\min\left\{ \frac{R_s + k_{ip}}{L_s}, \frac{P_G}{\left(i_f^P\right)^2 L_f} \right\} + \min\left\{ \frac{P_b - P_0}{\left(v_{dc}^P\right)^2 C_{dc}}, -\frac{P^P}{\left(v_f^P\right)^2 C_f} \right\} > 0 \tag{34}$$

To guarantee stable operations of the islanded hybrid AC/DC microgrids when a SPGF occurs, the positive-sequence stability criterion in (34) gives quantitative constraints on the positive-sequence power P_G of the PV unit, DC/AC converter current inner-loop proportional parameter k_{ip}, inductors L_s and L_f, inductor equivalent resistance R_s, energy storage unit power P_b, CPLs power P_0, capacitors C_d and C_f, DC bus voltage v_{dc}, and positive-sequence equivalent impulse power P^P of the SPGF.

3.3. Large Signal Model and Stability Criterion for Zero-Sequence Equivalent Model of Islanded Hybrid AC/DC Microgrids

The current and voltage variables are defined according to the zero-sequence equivalent model in Figure 12 and are shown as follows:

$$i = \begin{bmatrix} i_1^0 & i_g^0 \end{bmatrix}, v = \begin{bmatrix} v_s^0 & v_f^0 \end{bmatrix} \tag{35}$$

The power function ${P_i}^0$ associated with the current variables is as follows:

$$P_i^0 = -\frac{1}{2}\left(i_1^0\right)^2 R_1 - \frac{1}{2}\left(i_2^0\right)^2 R_2 - \frac{1}{2}\left(i_g^0\right)^2 R_g \tag{36}$$

The power function ${P_v}^0$ associated with the voltage variables is as follows:

$$P_v^0 = -P^0 + \int_0^{v_f^0} \frac{P^0}{v} dv \tag{37}$$

The power ${P^0}_{Cs}$, ${P^0}_{Cdc}$, ${P^0}_{Cf}$, and ${P^0}_{Cg}$ of capacitors C_s, C_{dc}, C_f, and C_g are as follows:

$$\begin{cases} P^0_{v_c} = i^0_1 v^0_c \\ P^0_{v_g} = i^0_g v^0_g \\ P^0_{v_s} = i^0_2 v^0_s - i^0_1 v^0_s \\ P^0_{v_f} = P^0_0 - i^0_2 v^0_f - i^0_g v^0_f \end{cases} \tag{38}$$

Combining (36)–(38), the mixed potential function $P(i^0,v^0)$ based on the zero-sequence equivalent model in Figure 12 is achieved and shown as follows:

$$\begin{gathered} P\left(i^0, v^0\right) = -\tfrac{1}{2}\left(i^0_1\right)^2 R_1 - \tfrac{1}{2}\left(i^0_2\right)^2 R_2 - \tfrac{1}{2}\left(i^0_g\right)^2 R_g + \int_0^{v^0_f} \tfrac{P^0}{v} dv + \\ i^0_1\left(v^0_c - v^0_s\right) + i^0_2\left(v^0_s - v^0_f\right) + i^0_g\left(v^0_g - v^0_f\right) \end{gathered} \tag{39}$$

Similarly, the large-signal stability criterion for a zero-sequence equivalent model of the islanded hybrid AC/DC microgrids is derived and shown as follows:

$$\min\left\{\frac{R_1}{L_1}, \frac{R_g}{L_g}\right\} - \frac{P^0}{\left(v^0_f\right)^2 C_f} > 0 \tag{40}$$

The constraints in (40) are related to the line equivalent resistance R_1, line equivalent inductance L_1, capacitance C_f, the equivalent inductance L_g in the faulty branch, the equivalent resistance R_g in the faulty branch, and zero-sequence equivalent impulse power P^0.

3.4. Combined Stability Criteria for Islanded Hybrid AC/DC Microgrids When SPGF Occurs

When a SPGF occurs, based on (34) and (40), the large-signal stability criteria of the islanded hybrid AC/DC microgrids are obtained and shown as follows:

$$\begin{cases} \min\left\{\frac{R_s + k_{ip}}{L_s}, \frac{P_G}{\left(i^P_f\right)^2 L_f}\right\} + \min\left\{\frac{P_b - P_0}{\left(v^P_{dc}\right)^2 C_{dc}}, -\frac{P^P}{\left(v^P_f\right)^2 C_f}\right\} > 0 \\ \min\left\{\frac{R_1}{L_1}, \frac{R_g}{L_g}\right\} - \frac{P^0}{\left(v^0_f\right)^2 C_f} > 0 \end{cases} \tag{41}$$

When a SPGF occurs, the maximum CPL power P_0 that the islanded hybrid AC/DC microgrids could stably support is derived from (41) and shown in (42).

$$P_0 < \left[\min\left(\frac{R_s + k_{ip}}{L_s}, \frac{P_G}{\left(i^P_f\right)^2 L_f}\right)\right]\left(v^P_{dc}\right)^2 C_{dc} + P_b \tag{42}$$

According to (42), if the variable CPLs power P_0 is always lower than the maximum power, islanded hybrid AC/DC microgrids stably operate as a SPGF occurs. In addition, with an increase in the PV unit power P_G, energy storage unit discharging power P_b, the current inner-loop proportional parameter k_{ip} of the bidirectional DC/AC converter and DC capacitor C_{dc}, the maximum CPL power that the islanded hybrid AC/DC microgrids could support increases. On the contrary, when the filter inductors L_s and L_f increase, the maximum CPL power that islanded hybrid AC/DC microgrids could support decreases. When a SPGF occurs, if the CPL power increases, in order to guarantee stable operation, the discharging power of the energy storage unit is increased. Unfortunately, if the discharging power of the energy storage unit cannot increase, load shedding appears. Inequality (42) provides important stable operation constants of the islanded hybrid AC/DC microgrids when a SPGF occurs.

Based on (41), to guarantee the stable operation of islanded hybrid AC/DC microgrids, the maximum positive-sequence impulse power and the maximum zero-sequence impulse power of a SPGF are also deduced and shown as follows:

$$\begin{cases} P^P < \left[\min\left\{\frac{R_s+k_{ip}}{L_s}, \frac{P_G}{\left(i_f^P\right)^2 L_f}\right\}\right]\left(v_f^P\right)^2 C_f \\ P^0 < \left[\min\left\{\frac{R_1}{L_1}, \frac{R_g}{L_g}\right\}\right]\left(v_f^0\right)^2 C_f \end{cases} \tag{43}$$

According to (43), if the positive-sequence impulse power P^P and zero-sequence impulse power P^0 are always lower than the maximum values, islanded hybrid AC/DC microgrids operate stably. In addition, with an increase in the current inner-loop proportional parameter k_{ip} of the bidirectional DC/AC converter, inductor equivalent resistance $R_{s,}$ and the positive-sequence power P_G of PV unit, the maximum positive-sequence impulse power that islanded hybrid AC/DC microgrids could stably suffer increases. On the contrary, when filter inductors L_s and L_f increase, the maximum positive-sequence impulse power that islanded hybrid AC/DC microgrids could stably suffer decreases. Similarly, with an increase in filter capacitor C_f, line equivalent resistance R_1, and inductor equivalent internal resistance R_g, the maximum zero-sequence impulse power that islanded hybrid AC/DC microgrids could stably suffer increases. On the contrary, when line equivalent inductance L_1 increases, the zero-sequence impulse power that islanded hybrid AC/DC microgrids could stably suffer decreases.

According to (13), the fault impulse power $S_p = P^P + P^0$. Consequently, the maximum impulse power of a SPGF that islanded hybrid AC/DC microgrids could stably suffer is derived from (43). It is concluded that inequality (43) offers extremely important guidelines for protection equipment.

4. Simulation Validation

To verify the correctness of the proposed large-signal stability criteria in (41), according to Figure 1, a simulation model of the islanded hybrid AC/DC microgrids is constructed using the MATLAB R2020a/Simulink software. *Q/V* and *P/f* droop controls are used for the bidirectional DC/AC converter. PI control strategies are utilized in the outer voltage controller and inner current controllers of the batteries' cascaded DC/DC converter. The CPLs are modeled by a closed loop-controlled buck converter and a resistor. DC/DC converters cascaded with AC/DC converters are utilized in PV units to achieve the power output. When a SPGF occurs in a PV unit, the fault impulse power is injected at the fault point. This procedure is simulated by sudden load power steps.

The simulation parameters of the islanded hybrid AC/DC microgrids are shown in Table 1. The DC bus voltage is 650 V, the AC bus voltage is 311 V, the initial power of the CPLs is 30 kW, and the power of the PV power generation unit is 5 kW.

Table 1. Simulation parameters of islanded hybrid AC/DC microgrids.

Representations/Unit	Value
The voltage of AC bus, v_{abc}/V	311
The voltage of DC bus, v_{dc}/V	650
The voltage of batteries, v_b/V	400
The AC filter inductance, L_s/mH	5
The AC filter capacitance, C_s/μF	100
The DC capacitor, C_{dc}/μF	500
The distributed power, P_V/kW	5
DC/AC converter current loop scaling factor for energy storage units, k_{ip}	0.1
The droop coefficients, m, n	$m = 1 \times 10^{-5}$, $n = 3 \times 10^{-4}$

According to (41) and Table 1, the large-signal stability criteria of the islanded hybrid AC/DC microgrids when a SPGF occurs are as follows:

$$\frac{R_s + k_{ip}}{L_s} - \frac{P^{\mathrm{P}}}{\left(v_f^{\mathrm{P}}\right)^2 C_f} + \frac{R_1}{L_1} - \frac{P^0}{\left(v_f^0\right)^2 C_f} > 0 \tag{44}$$

Then, the maximum fault impulse power of a SPGF that the islanded hybrid AC/DC microgrids could stably suffer is 38.37 kW and is shown as

$$P^{\mathrm{P}} + P^0 < 38.37 \text{ kW} \tag{45}$$

In order to verify the correctness of (45), the parameters of the two groups are designed and shown in Table 2. Group A satisfies (45), while Group B does not.

Table 2. The parameters of simulations A and B.

Group	A	B
Initial and final values of power steps (kW)	3–35	3–40
Satisfying the proposed large-signal stability criteria	YES	NO

At 0.5 s, a SPGF appears in the AC side of the islanded hybrid AC/DC microgrids. To simulate this procedure, the power steps of Group A are from 3 kW to 35 kW, and the power steps of Group B are from 3 kW to 40 kW.

When parameters in Group A are utilized, the waveforms of power steps, energy storage unit power, DC bus voltage, and AC bus voltage are shown in Figures 13–16. As the fault impulse power of a SPGF increases from 3 kW to 35 kW, tend to stabilize after power step, and the charging state of the energy storage unit is changed into a discharging state. After a drop, the DC bus voltage recovers to 650 V at 0.9 s, and the AC bus voltage also returns to 311 V at 0.6 s behind a small fluctuation. Figures 13–16 illustrate that the parameters of Group A could guarantee islanded hybrid AC/DC microgrid stability when a SPGF occurs.

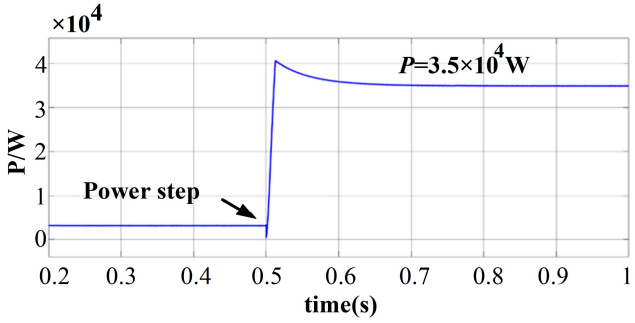

Figure 13. The waveforms of power steps when Group A is utilized.

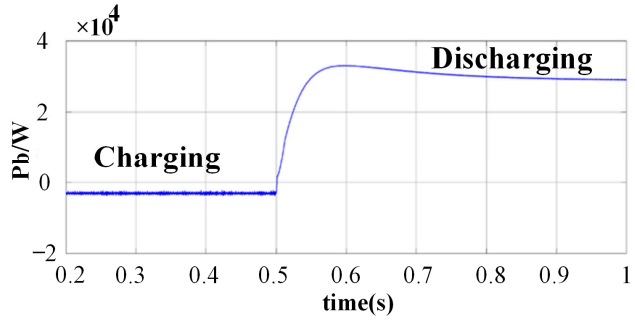

Figure 14. The power of energy storage unit when Group A is utilized.

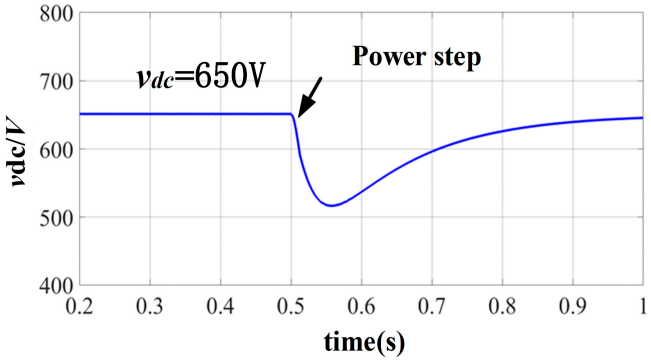

Figure 15. The waveform of DC bus voltage when Group A is utilized.

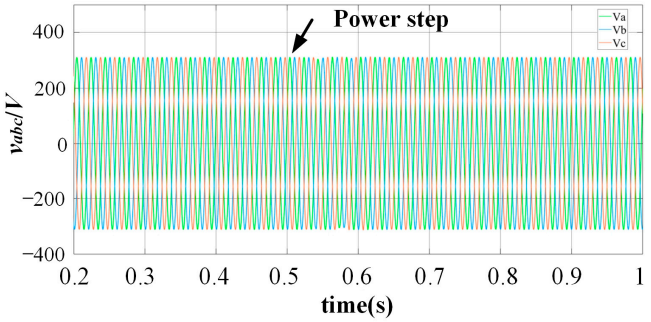

Figure 16. The waveform of AC bus voltage when Group A is utilized.

Then, when the parameters in Group B are adopted, the waveforms of power steps, energy storage unit power, DC bus voltage, and AC bus voltage are shown in Figures 17–20. As the fault impulse power of the SPGF increases from 3 kW to 40 kW, violent oscillations appear in power steps and energy storage unit power, and the DC bus voltage oscillates significantly between 2 kV and 0 V. At 0.5 s, slight oscillations present in the AC voltage. At 0.6 s, the AC voltage is seriously distorted and cannot restore stability. Figures 17–20 demonstrate that the parameters of Group B could not guarantee islanded hybrid AC/DC microgrid stability when a SPGF occurs.

The simulation result comparisons of Figures 13–20 indicate that the parameters satisfying (45) could guarantee islanded hybrid AC/DC microgrid stability when a SPGF occurs, while parameters not satisfying (45) could not ensure islanded hybrid AC/DC microgrid stability when a SPGF occurs. The simulation results verify the validity of the derived large-signal stability criteria in (41).

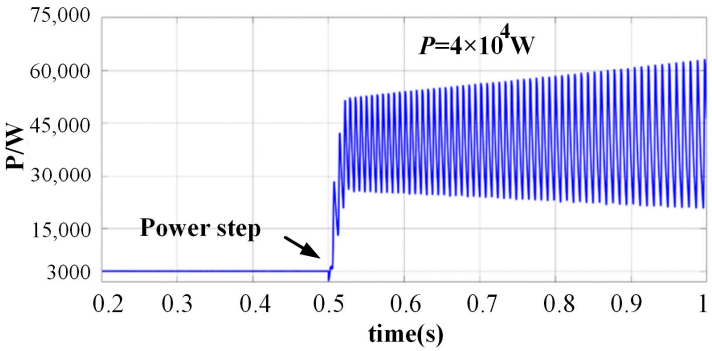

Figure 17. The waveform of power steps when Group B is utilized.

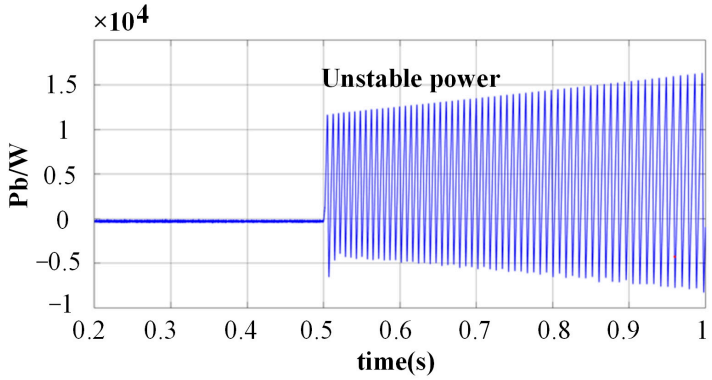

Figure 18. The power of energy storage unit when Group B is utilized.

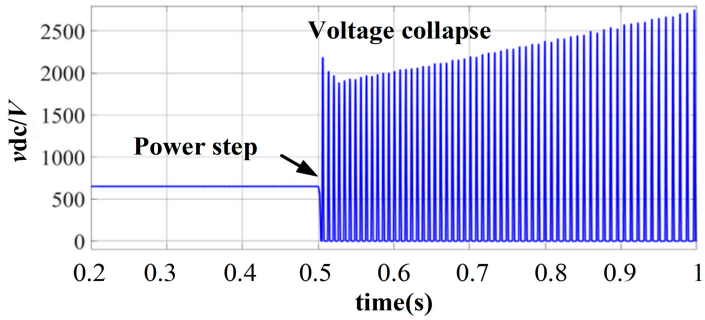

Figure 19. The waveform of DC bus voltage when Group B is utilized.

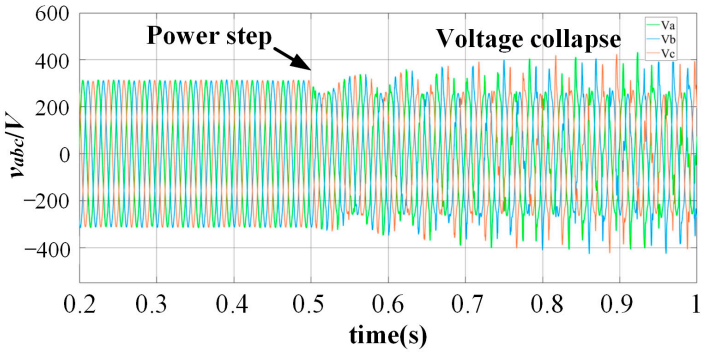

Figure 20. The waveform of AC bus voltage when Group B is utilized.

5. Experimental Validation

To verify the proposed large-signal stability criteria in (41), according to Figure 1, a prototype of the islanded hybrid AC/DC microgrids is built using the PTS-5000 experimental platform, Good Will Instrument (Suzhou) Co., Ltd., Suzhou, China, as shown in Figure 21. The experimental platform consists of the controller TMS320F28335, DC/DC converters, DC/AC converters, constant power loads (CPLs), AC resistive load, the power source, and the oscilloscope. Droop controls are used for the bidirectional DC/AC converters. Outer voltage controllers and inner current controllers are utilized in battery-cascaded DC/DC converters. The PV unit is represented by the power source. Load power steps are also utilized to perform the impulse power of a SPGF. The parameters of the experimental prototype are shown in Table 3.

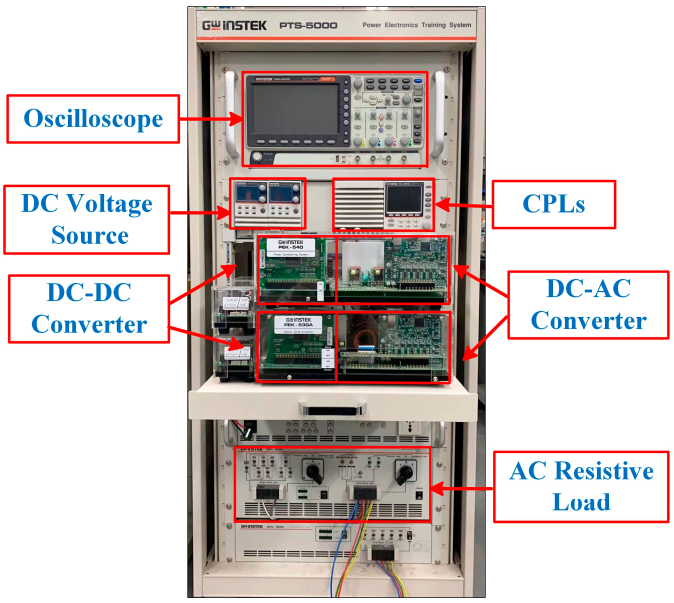

Figure 21. Experimental platform of AC/DC hybrid microgrids with CPLs.

Table 3. Experimental parameters of islanded hybrid AC/DC hybrid microgrids.

Representations/Unit	Value
The voltage of AC bus, v_{abc}/V	20
The voltage of DC bus, v_{dc}/V	60
The voltage of batteries, v_b/V	40
The AC filter inductance, L_s/mH	1
The AC filter capacitance, C_s/μF	10
The DC capacitor, C_{dc}/μF	470
The output power of PV unit, P_G/W	40
The outer voltage control loop parameters of bidirectional DC/AC converter, k_{vp}, k_{vi}	$k_{vp} = 0.6$, $k_{vi} = 0.1$
The inner current control loop parameters of bidirectional DC/AC converter, k_{ip}, k_{ii}	$k_{ip} = 2$, $k_{ii} = 0.1$

Similarly, based on (41) and Table 3, the maximum fault impulse power of a SPGF that the islanded hybrid AC/DC microgrids could stably suffer is 91.37 W. The parameters of the two groups are also designed and shown in Table 4. The powers of Group C are less than 91.37 W, while the powers of Group D are more than 91.37 W.

Table 4. The experimental parameters of groups C and D.

Group	C	D
Initial and final values of power steps (W)	30–80	30–100
Satisfying the proposed large-signal stability criteria	YES	NO

When the parameters in Group C are utilized, the waveforms of the AC bus voltage and current are shown in Figure 22, and the DC bus voltage and the energy storage current are shown in Figure 23. As the fault impulse power of the SPGF increases from 30 W to 80 W, the AC bus voltage maintains stable operation after a small fluctuation, and the DC bus voltage also returns to 60 V after a transient drop, while the output current of the energy storage unit increases and then operates steadily. The results in Figures 22 and 23 coincide with the simulation results in Figures 13–16. Figures 22 and 23 illustrate that the parameters of Group C could guarantee that islanded hybrid AC/DC microgrids are stable when a SPGF occurs.

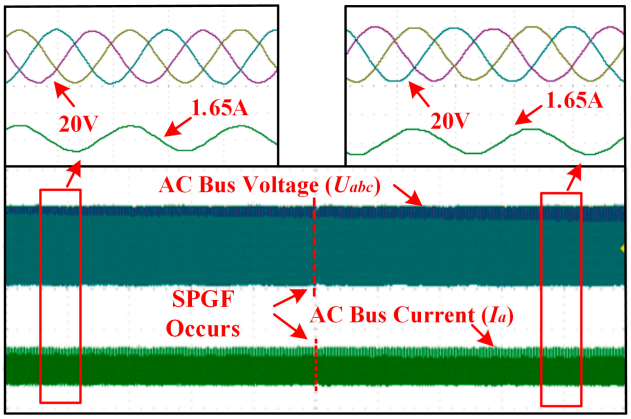

Figure 22. Waveforms of AC bus voltage and current when Group C is utilized.

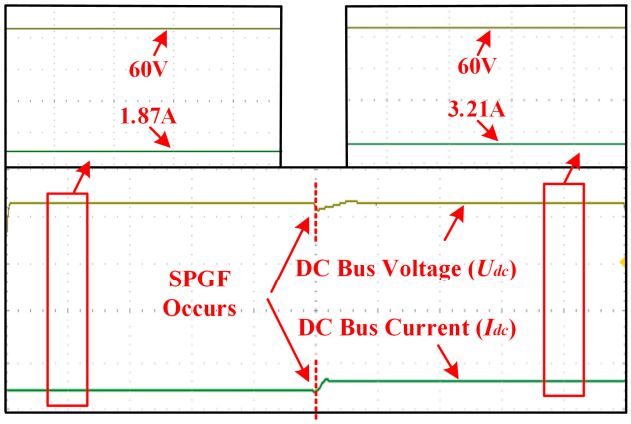

Figure 23. Waveforms of DC bus voltage and the energy storage current when Group C is utilized.

Then, when the parameters in Group D are adopted, the waveforms of the AC bus voltage and current are shown in Figure 24, and the DC bus voltage and the energy storage current are shown in Figure 25. As the fault impulse power of the SPGF increases from 30 W to 100 W, serious distortions appear in the AC bus voltage and current waveforms, while the DC bus voltage drops from 60 V to 49.51 V and does not recover to 60 V. The results in Figures 24 and 25 coincide with the simulation results in Figures 17–20. Figures 24 and 25 demonstrate that the parameters of Group D could not guarantee islanded hybrid AC/DC microgrid stability when a SPGF occurs.

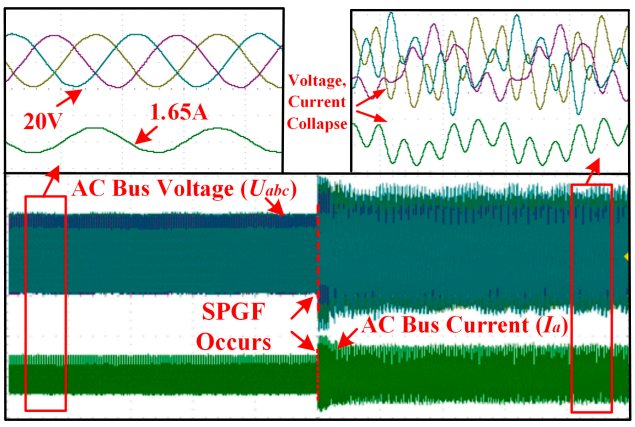

Figure 24. Waveforms of AC bus voltage and current when Group D is utilized.

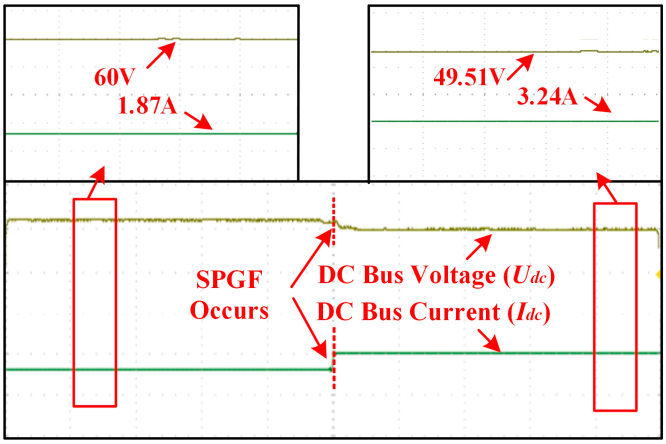

Figure 25. Waveforms of DC bus voltage and the energy storage current when Group D is utilized.

The experimental result comparisons of Figures 22–25 illustrate that the parameters satisfying (41) could guarantee the islanded hybrid AC/DC microgrid's stability when a SPGF occurs, while the parameters not satisfying (41) could not ensure the islanded hybrid AC/DC microgrid's stability when a SPGF occurs. These experimental results show the correctness of the derived large-signal stability criteria in (41).

The experimental results and simulation results all prove the validity of the proposed large-signal stability criteria of the islanded hybrid AC/DC microgrids when a SPGF occurs, as shown in (41).

6. Conclusions

Firstly, based on the structure and control strategies, the method of symmetrical components is utilized, and the positive-sequence equivalent model and zero-sequence equivalent model of islanded AC/DC hybrid microgrids when a SPGF occurs are derived separately. Then, the mixed potential theory is utilized, and large-signal stability criteria of the islanded hybrid AC/DC microgrids when a SPGF occurs are obtained. The proposed stability criteria in (41) give quantitative constraints on the positive-sequence power P_G of the PV unit, DC/AC converter current inner-loop proportional parameter k_{ip}, inductors L_s and L_f, inductor equivalent resistance R_s, energy storage unit power P_b, CPLs power P_0, capacitors C_d and C_f, DC bus voltage v_{dc}, the line equivalent resistance R_1, line equivalent inductance L_1, capacitance C_f, the equivalent inductance L_g in the faulty branch, the equivalent resistance R_g in the faulty branch, the positive-sequence equivalent impulse power P^P of SPGF, and zero-sequence equivalent impulse power P^0. The stability influences of these parameters are sufficiently analyzed, and the maximum power of the CPLs that islanded hybrid AC/DC microgrids could stably support as the SPGF occurs is obtained. Simultaneously, to guarantee the stable operation of islanded hybrid AC/DC microgrids, the maximum impulse power of a SPGF is also deduced. Finally, simulation and experimental validations are performed, and prove the correctness of the derived large-signal stability criteria.

The derived maximum impulse power of a SPGF that the islanded hybrid AC/DC microgrids could stably suffer is extremely important and provides quantitative guidelines for protection equipment to decide when to work. Furthermore, if the impulse power of a SPGF is less than the maximum power, islanded hybrid AC/DC microgrids could work under a SPGF. Then, the allowable maximum CPL power that islanded hybrid AC/DC microgrids could stably support as the SPGF occurs is deduced, and the power is usually adopted to determine the power of the energy storage unit and load shedding in advance.

The presented large-signal stability criteria of islanded hybrid AC/DC microgrids when a SPGF occurs are essential for achieving power allocation and guaranteeing stable operation.

Author Contributions: Study design, literature search, and manuscript writing, X.L.; graph production, data analysis, and data processing, Y.Z.; supervision; resources, and review and editing, X.S.; translation and literature search, Y.J. All authors have read and agreed to the published version of the manuscript.

Funding: This project is supported by the National Natural Science Foundation of China (52237008).

Data Availability Statement: Data are available from the authors.

Conflicts of Interest: The authors declare no conflicts of interest.

References

1. Gupta, A.; Doolla, S.; Chatterjee, K. Hybrid AC–DC Microgrid: Systematic Evaluation of Control Strategies. *IEEE Trans. Smart Grid* **2018**, *9*, 3830–3843. [CrossRef]
2. Lasseter, R.H. MicroGrids. In Proceedings of the 2002 IEEE Power Engineering Society Winter Meeting. Conference Proceedings (Cat. No. 02CH37309), New York, NY, USA, 27–31 January 2002; Volume 1, pp. 305–308.
3. Sadabadi, M.S.; Shafiee, Q. Scalable Robust Voltage Control of DC Microgrids With Uncertain Constant Power Loads. *IEEE Trans. Power Syst.* **2020**, *35*, 508–515. [CrossRef]
4. Karimipour, D.; Salmasi, F.R. Stability Analysis of AC Microgrids With Constant Power Loads Based on Popov's Absolute Stability Criterion. *IEEE Trans. Circuits Syst. II Express Briefs* **2015**, *62*, 696–700. [CrossRef]
5. Hassan, M.A.; Su, C.-L.; Pou, J.; Sulligoi, G.; Almakhles, D.; Bosich, D.; Guerrero, J.M. DC Shipboard Microgrids with Constant Power Loads: A Review of Advanced Nonlinear Control Strategies and Stabilization Techniques. *IEEE Trans. Smart Grid* **2022**, *13*, 3422–3438. [CrossRef]
6. Borrell, Á.; Velasco, M.; Castilla, M.; Miret, J.; Guzmán, R. Collaborative Voltage Unbalance Compensation in Islanded AC Microgrids With Grid-Forming Inverters. *IEEE Trans. Power Electron.* **2022**, *37*, 10499–10513. [CrossRef]
7. Tian, Z.; Li, X.; Zha, X.; Tang, Y.; Sun, P.; Huang, M.; Yu, P. Transient Synchronization Stability of an Islanded AC Microgrid Considering Interactions Between Grid-Forming and Grid-Following Converters. *IEEE J. Emerg. Sel. Top. Power Electron.* **2023**, *11*, 4463–4476. [CrossRef]
8. Mohammadi, J.; Ajaei, F.B.; Stevens, G. Grounding the AC Microgrid. *IEEE Trans. Ind. Appl.* **2019**, *55*, 98–105. [CrossRef]
9. Acharya, J.R.; Wang, Y.; Xu, W. Temporary Overvoltage and GPR Characteristics of Distribution Feeders with Multigrounded Neutral. *IEEE Trans. Power Deliv.* **2010**, *25*, 1036–1044. [CrossRef]
10. Zeng, X.; Yu, K.; Wang, Y.; Xu, Y. A novel single phase grounding fault protection scheme without threshold setting for neutral ineffectively earthed power systems. *CSEE J. Power Energy Syst.* **2016**, *2*, 73–81. [CrossRef]
11. Barik, M.A.; Gargoom, A.; Mahmud, M.A.; Haque, M.E.; Al-Khalidi, H.; Oo, A.M.T. A Decentralized Fault Detection Technique for Detecting Single Phase to Ground Faults in Power Distribution Systems With Resonant Grounding. *IEEE Trans. Power Deliv.* **2018**, *33*, 2462–2473. [CrossRef]
12. Yuan, W.; Li, Y.; Xu, L.; Li, T.; Chen, X. A Fast Faulty Phase Selection Method Considering Fault Tolerance for Single Phase to Ground Fault in Distribution Networks. *IEEE Trans. Instrum. Meas.* **2023**, *72*, 1–12. [CrossRef]
13. Alluraiah, N.C.; Vijayapriya, P. Optimization, Design, and Feasibility Analysis of a Grid-Integrated Hybrid AC/DC Microgrids for Rural Electrification. *IEEE Access* **2023**, *11*, 67013–67029. [CrossRef]
14. Ma, S.; Geng, H.; Liu, L.; Yang, G.; Pal, B.C. Grid-Synchronization Stability Improvement of Large Scale Wind Farm During Severe Grid Fault. *IEEE Trans. Power Syst.* **2018**, *33*, 216–226. [CrossRef]
15. Tang, W.; Hu, J.; Chang, Y.; Liu, F. Modeling of DFIG-Based Wind Turbine for Power System Transient Response Analysis in Rotor Speed Control Timescale. *IEEE Trans. Power Syst.* **2018**, *33*, 6795–6805. [CrossRef]
16. Wu, H.; Wang, X. Design-Oriented Transient Stability Analysis of PLL-Synchronized Voltage-Source Converters. *IEEE Trans. Power Electron.* **2020**, *35*, 3573–3589. [CrossRef]
17. Liu, P.; Huang, C. Detecting Single-Phase-to-Ground Fault Event and Identifying Faulty Feeder in Neutral Ineffectively Grounded Distribution System. *IEEE Trans. Power Deliv.* **2018**, *33*, 2265–2273. [CrossRef]
18. Chen, J.; Li, H.; Deng, C.; Wang, G. Detection of Single-Phase to Ground Faults in Low-Resistance Grounded MV Systems. *IEEE Trans. Power Deliv.* **2021**, *36*, 1499–1508. [CrossRef]
19. Zhou, H.; Yao, W.; Sun, K.; Ai, X.; Wen, J.; Cheng, S. Characteristic Investigation and Overvoltage Suppression of MMC-HVDC Integrated Offshore Wind Farms Under Onshore Valve-Side SPG Fault. *IEEE Trans. Power Syst.* **2024**, *39*, 1346–1359. [CrossRef]
20. Taul, M.G.; Wang, X.; Davari, P.; Blaabjerg, F. An Overview of Assessment Methods for Synchronization Stability of Grid-Connected Converters Under Severe Symmetrical Grid Faults. *IEEE Trans. Power Electron.* **2019**, *34*, 9655–9670. [CrossRef]
21. Piya, P.; Ebrahimi, M.; Karimi-Ghartemani, M.; Khajehoddin, S.A. Fault Ride-Through Capability of Voltage-Controlled Inverters. *IEEE Trans. Ind. Electron.* **2018**, *65*, 7933–7943. [CrossRef]
22. Cheng, H.; Shuai, Z.; Shen, C.; Liu, X.; Li, Z.; Shen, Z.J. Transient Angle Stability of Paralleled Synchronous and Virtual Synchronous Generators in Islanded Microgrids. *IEEE Trans. Power Electron.* **2020**, *35*, 8751–8765. [CrossRef]
23. Sadeghkhani, I.; Golshan, M.E.H.; Guerrero, J.M.; Mehrizi-Sani, A. A Current Limiting Strategy to Improve Fault Ride-Through of Inverter Interfaced Autonomous Microgrids. *IEEE Trans. Smart Grid* **2017**, *8*, 2138–2148. [CrossRef]

24. Taul, M.G.; Wang, X.; Davari, P.; Blaabjerg, F. Current Limiting Control With Enhanced Dynamics of Grid-Forming Converters During Fault Conditions. *IEEE J. Emerg. Sel. Top. Power Electron.* **2020**, *8*, 1062–1073. [CrossRef]
25. Zarei, S.F.; Ghasemi, M.A.; Peyghami, S.; Blaabjerg, F. A Fault Detection Scheme for Islanded-Microgrid with Grid-Forming Inverters. In Proceedings of the 2021 6th IEEE Workshop on the Electronic Grid (eGRID), New Orleans, LA, USA, 8–10 November 2021; pp. 1–6. [CrossRef]
26. He, L.; Li, Y.; Chu, X.; Shuai, Z.; Peng, Y.; Shen, Z.J. Single-Phase to Ground Fault Line Identification for Medium Voltage Islanded Microgrids With Neutral Ineffectively Grounded Modes. *IEEE Trans. Smart Grid* **2022**, *13*, 4312–4326. [CrossRef]
27. Xie, W.; Han, M.; Cao, W.; Guerrero, J.M.; Vasquez, J.C. System-Level Large signal Stability Analysis of Droop-Controlled DC Microgrids. *IEEE Trans. Power Electron.* **2021**, *36*, 4224–4236. [CrossRef]
28. Kabalan, M.; Singh, P.; Niebur, D. A Design and Optimization Tool for Inverter-Based Microgrids Using Large signal Nonlinear Analysis. *IEEE Trans. Smart Grid* **2019**, *10*, 4566–4576. [CrossRef]
29. Huang, T.; Gao, S.; Xie, L. A Neural Lyapunov Approach to Transient Stability Assessment of Power Electronics-Interfaced Networked Microgrids. *IEEE Trans. Smart Grid* **2022**, *13*, 106–118. [CrossRef]
30. Severino, B.; Strunz, K. Enhancing Transient Stability of DC Microgrids by Enlarging the Region of Attraction Through Nonlinear Polynomial Droop Control. *IEEE Trans. Circuits Syst. I Regul. Pap.* **2019**, *66*, 4388–4401. [CrossRef]
31. Liu, X.; Sun, X. Large Signal Stability analysis of Hybrid AC/DC Microgrids Based on T-S fuzzy model method. In Proceedings of the 2019 22nd International Conference on Electrical Machines and Systems (ICEMS), Harbin, China, 11–14 August 2019; pp. 1–6. [CrossRef]
32. Liu, X.; Li, Z.; Song, X.; Zhou, J.; Qu, Y. Large signal stability criterion of AC–DC hybrid Microgrids with constant power loads considering reference current limitation. *IET Gener. Transm. Distrib.* **2022**, *16*, 4589–4599. [CrossRef]
33. Liu, Z.; Ge, X.; Su, M.; Han, H.; Xiong, W.; Gui, Y. Complete Large signal Stability Analysis of DC Distribution Network via Brayton-Moser's Mixed Potential Theory. *IEEE Trans. Smart Grid* **2023**, *14*, 866–877. [CrossRef]
34. Wu, Z.; Han, H.; Liu, Z.; Su, M.; Sun, Y.; Zhang, X.; Wang, P. A Novel Method for Estimating the Region of Attraction for DC Microgrids via Brayton-Moser's Mixed Potential Theory. *IEEE Trans. Smart Grid* **2023**, *14*, 3313–3316. [CrossRef]
35. Allam, M.A.; Hamad, A.A.; Kazerani, M. A Sequence-Component-Based Power-Flow Analysis for Unbalanced Droop-Controlled Hybrid AC/DC Microgrids. *IEEE Trans. Sustain. Energy* **2019**, *10*, 1248–1261. [CrossRef]
36. Brayton, R.K.; Moser, J.K. A theory of nonlinear networks: I. *Q. Appl. Math.* **1964**, *22*, 1–33. [CrossRef]
37. Weiss, L.; Mathis, W.; Trajkovic, L. A generalization of Brayton-Moser's mixed potential function. *IEEE Trans. Circuits Syst. I Fundam. Theory Appl.* **1998**, *45*, 423–427. [CrossRef]
38. Jeltsema, D.; Scherpen, J.M.A. On Brayton and Moser's missing stability theorem. *IEEE Trans. Circuits Syst. II Express Briefs* **2005**, *52*, 550–552. [CrossRef]
39. Chang, F.; Cui, X.; Wang, M.; Su, W.; Huang, A.Q. Large signal Stability Criteria in DC Power Grids With Distributed-Controlled Converters and Constant Power Loads. *IEEE Trans. Smart Grid* **2020**, *11*, 5273–5287. [CrossRef]